Geothermics 91 (2021) 101976

Contents lists available at ScienceDirect

Geothermics

journal homepage: www.elsevier.com/locate/geothermics

Effects of fault transmissivity on the potential of fault reactivation and induced seismicity: Implications for understanding induced seismicity at Pohang EGS

B.B.T Wassing [a,*], Q. Gan [b], T. Candela [a], P.A. Fokker [a]

[a] TNO Applied Geoscience, Utrecht, the Netherlands
[b] University of Aberdeen, Aberdeen, Scotland, United Kingdom

ARTICLE INFO

Keywords:
Induced seismicity
Fault reactivation
Hydraulic stimulation
Enhanced geothermal systems
Pore pressure diffusion
Poroelasticity
Pohang EGS

ABSTRACT

Enhanced Geothermal Systems (EGS) involve hydraulic stimulation of the permeability of deep low-permeable rock formations. This causes the reactivation and opening of pre-existing natural fracture networks and the formation of new fractures. During hydraulic stimulation, injection pressures at the bottom of the injection well can reach overpressures of up to several tens of MPa. The associated rise in reservoir pressures may trigger felt induced seismicity, as large-scale critically stressed fault structures can be reactivated. We here employ a 3D hydro-mechanical model coupling the software codes of TOUGHREACT and FLAC3D and combine it with Dieterich's formulation for the rate of earthquake nucleation, to create a conceptual model to simulate the effect of stimulation activities on fault Coulomb stressing and associated induced seismicity rates. We discuss the effect of the hydromechanical properties such as fault and damage zone transmissivity and elastic properties on the relative contribution of pore pressure diffusion versus poroelasticity to fault loading. Our modelling approach shows that poroelastic effects can significantly contribute to fault loading, specifically in cases of low fault transmissivity. In this context, we discuss the potential contribution of poroelasticity to the occurrence of seismicity on a previously unmapped sealing fault associated to hydraulic stimulation at the Pohang EGS site in the Southeast of Korea. Our study demonstrates that a quantitative understanding of the stress response and induced seismicity upon injection operations such as the hydraulic stimulation at Pohang requires the incorporation of both pore pressure diffusion and poroelastic effects.

1. Introduction

In Enhanced Geothermal Systems the permeability of deep low-permeability rocks is increased by hydraulic stimulation. One of the downsides of hydraulic stimulation is that the increase in pore pressures will affect fault stress states and may trigger or induce felt seismicity. Examples of earthquakes which have been related to hydraulic stimulation for Enhanced Geothermal Systems are the 2006 M_w 3.4 earthquake which occurred some days after hydraulic stimulation activities at the Basel EGS site in Switzerland (Deichmann et al., 2014), the 2003 M_L 3.7 earthquake related to stimulation of the Habanero wells in Cooper Basin, Australia (Baisch et al., 2006), and the 2003 M_w 2.9 earthquake at the EGS site of Soultz-sous-Forêts, France (Dorbath et al., 2009). More recently, a magnitude M_w 5.5 seismic event was reported close to the geothermal site near Pohang in Korea. This event occurred on November 15th 2017, close to two injectors at the Pohang EGS site (Ge et al., 2019; Grigoli et al., 2018; Kim et al., 2018).

During hydraulic stimulation of EGS reservoirs, several (tens of) thousands cubic meters of fluids can be injected into the subsurface. In this context, a pending challenge is to disentangle the relative contribution of pore pressure diffusion and poroelastic effects on the loading of nearby faults. Indeed, the work of Segall and Lu (2015) has shown that the associated pore pressure diffusion and poroelastic effects can affect Coulomb stressing rates on faults close to injector wells. The two-dimensional plane-strain numerical study of Chang and Segall (2016) predicted that for low-permeability basement faults the poroelastic stresses, due to fluid injection into overlying strata, can be significant even without elevated pore pressure. Chang and Yoon (2018) showed that the presence of low-permeability sealing faults close to injectors can significantly influence the evolution of pore pressures and

* Corresponding author.
E-mail address: brecht.wassing@tno.nl (B.B.T Wassing).

https://doi.org/10.1016/j.geothermics.2020.101976
Received 11 November 2019; Received in revised form 17 September 2020; Accepted 23 September 2020
Available online 13 January 2021

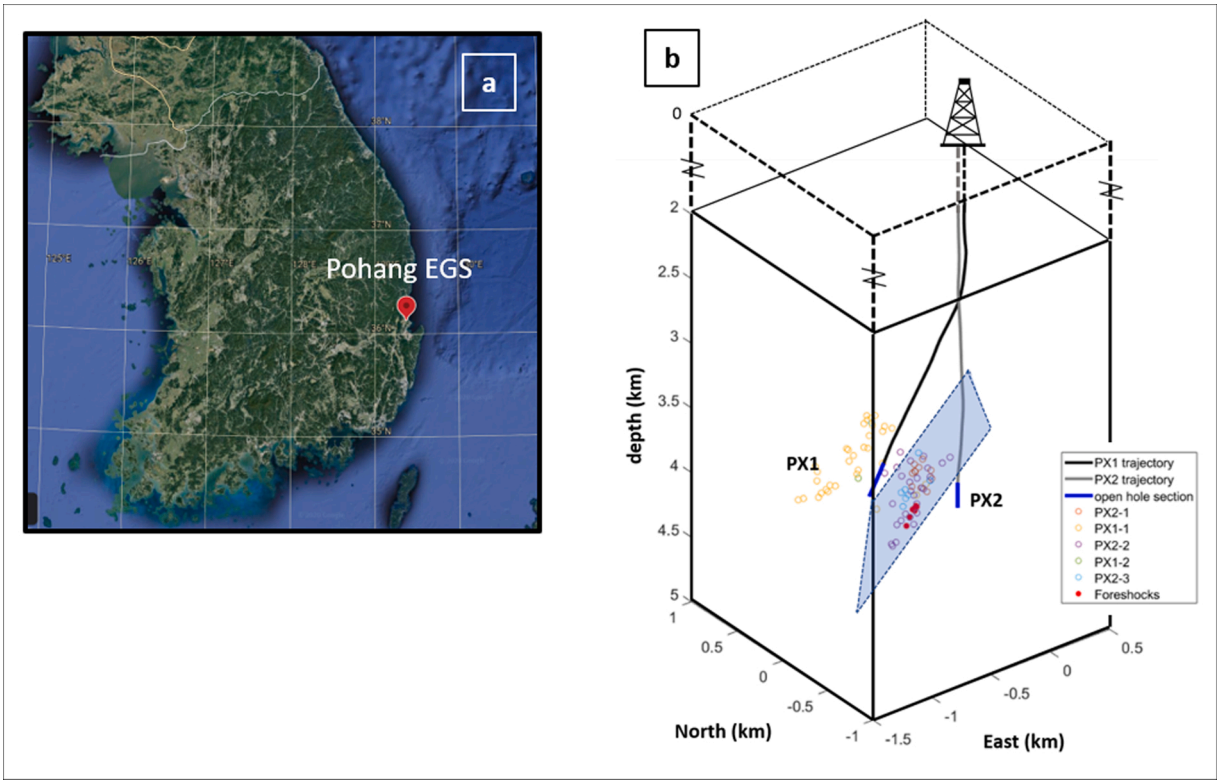

Fig. 1. a) Pohang EGS location and b) well trajectories of injection wells PX-1 and PX-2 and schematic presentation of the fault structure in between the wells PX-1 and PX-2. Small dots present locations of seismic events; different color-coding indicates stimulation phase that seismic events have been linked to (seismic event locations obtained from Ge et al., 2019).

poroelastic effects, thereby influencing fault reactivation and related seismicity. A recent paper by Chang et al. (2020) showed that prolonged accumulation of poroelastic strain and pore pressure diffusion may have caused seismic events of magnitudes $M_w > 3$ at the Pohang EGS site. On the other hand, Zbinden et al. (2020) found the direct pressure effect dominated the stress response on a fault nearby and hydraulically connected to the St. Gallen injection well.

We have analyzed the spatio-temporal pattern of stress changes and induced seismicity on fault structures of varying transmissivity close to an injector well. We employed a 3D hydro-mechanical model coupling TOUGHREACT with FLAC3D (based on Taron and Elsworth, 2010), in combination with Dieterich's formulation for earthquake nucleation rates (Dieterich, 1994). We built a conceptual model, in which we varied fault transmissivity, and compared the relative contributions of pore pressure diffusion and poroelasticity to fault loading. In our model, fault geometry, in-situ stresses, well configuration and the geological setting are based on the descriptions of the Pohang EGS site (Kim et al., 2018; Ge et al., 2019). A relation between the injection activities at the Pohang EGS site, and the occurrence of the seismicity has been discussed in several recent publications (Kim et al., 2018; Grigoli et al., 2018; Ge et al., 2019; Chang et al., 2020). Based on well test analysis, Ge et al. (2019) interpreted the fault that hosted the Mw 5.5 earthquake in Pohang as a sealing fault structure, located between the injectors at the Pohang EGS site. In this context, we discuss the potential contribution of poroelasticity to the occurrence of seismicity on this previously unmapped sealing fault between the injector wells. However, we emphasize that in this study we did not aim to derive a fully calibrated and validated model of the Pohang EGS stimulation activities. Instead, we have aimed for a conceptual understanding of what processes may have played a role in fault reactivation and induced seismicity, and how they may have affected the timing and location of induced seismicity at the Pohang EGS hydraulic stimulation site.

2. Background information on Pohang hydraulic stimulation

The two boreholes PX-1 and PX-2 at the Pohang injection site targeted fractured granodiorites in the basement rocks. A deviated production well (PX-1) and a vertical injection well (PX-2) had been drilled into the granitic basement down to depths of around 4.2–4.3 km, with open-hole sections at the bottom of the well, some 600 m apart. From January 29th 2016 to September 2017, both wells were alternatingly stimulated during five separate stages. A total cumulative volume of 12,800 m^3 of fluids was injected into the basement rocks, with a net volume of 6000 m^3 remaining in the rocks after bleed-off of the wells (Kim et al., 2018; Ge et al., 2019). Injection schemes in terms of applied injection rates, total and net injection volumes, continuity of injection (i.e. either continuous, stepped or cyclic) and maximum wellhead pressures varied widely between the different stimulation stages and the two injection wells (Park et al., 2017, Kim et al., 2018; Hofmann et al., 2019; Ge et al., 2019). Wellhead pressures up to 28 MPa and rates up to 18 L/s have been reported for the two PX-1 stimulations, whereas wellhead pressures up to 89 MPa and rates up to 47 L/s have been reported for the first two PX-2 stimulations. To date, little information on applied injection rates and maximum wellhead pressures has been published on the 5th and last stimulation stage, though Chang et al. (2020) report simultaneous injection-extraction activities in PX-1 and PX-2 for the last stimulation phase.

On November 15th 2017, around two months after the last stimulation, a magnitude M_w 5.5 event occurred on a NW 65−75° dipping large-scale fault structure at a distance of less than 1 km from the injection site (Grigoli et al., 2018; Kim et al., 2018). Grigoli et al. (2018); Kim et al. (2018) discuss the correlation between the timing and location of the mainshock and the injection activities and conclude that the large magnitude event was probably triggered by the stimulation activities. Fault gouge encountered during drilling of wellbore PX-2 indicates the presence of a fault intersecting PX-2 at a depth of around 3800 m,

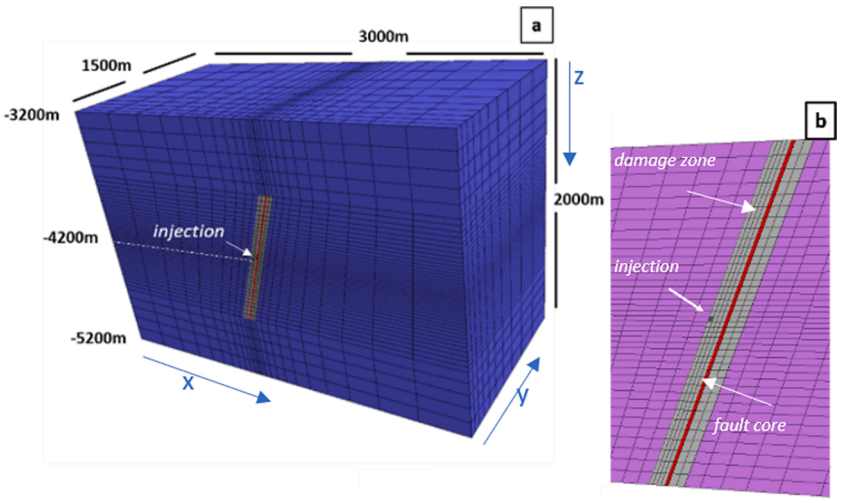

Fig. 2. a) Geometry of the fault (red), damage zone (grey) and matrix rocks (blue), for the base case scenario; b) Close-up of the fault zone and location of injection. Half of the model shown (model has been cut by a vertical plane oriented perpendicular to the y-axis, through the injection point). (For interpretation of the references to colour in this figure legend, the reader is referred to the web version of this article).

whereas well test analysis at the Pohang site shows evidence of a low-permeability fault structure likely to be present between the two injectors, with PX-1 in the hanging wall block and PX-2 in the footwall block (Ge et al., 2019). Fig. 1 gives a schematic overview of the well configuration at the Pohang EGS site.

3. Modelling approach

We performed the numerical simulations with a 3D hydro-mechanical model coupling the flow simulator of TOUGHREACT with the geomechanical simulator of FLAC3D, following the original approach described by Taron et al., 2010. Though TOUGHREACT can be used for modelling thermo-hydro-mechanical and coupled chemical processes, in our approach we did not model the chemical reaction processes and only used the multiphase flow part of the code, which is based on TOUGH2. For every time step in the numerical simulation, pore pressures computed in TOUGHREACT are passed on to FLAC3D to determine associated changes in stress and strain. Changes in stress and strain are then sent back to TOUGHREACT and used to update porosity, (optionally) permeability and pore pressures due to deformation. The value of the Biot coefficient determines the amount of coupling between pore pressure changes derived from TOUGHREACT and the poroelastic stress and strain in FLAC3D.

We constructed the 3D hydro-mechanical model based on descriptions of the fault zone structures in Caine et al. (1996); Mitchell and Faulkner (2009) and Choi et al. (2015). The model consists of a fault, surrounded by a high-permeability damage zone, all embedded in a low-permeability matrix (Fig. 2). The situation of the Pohang EGS site served as basis for our conceptual model. The base scenario simulates injection into a single well, that resembles the position of PX-1 in the hanging wall block of a sealing fault. The fault is located at a depth between 3700 m and 4700 m below surface. Fault dimensions are 1000 m (height) by 3000 m (width) and the fault dip is 70°, based on the focal mechanism derived for the Mw 5.5 mainshock in Pohang (Grigoli et al., 2018). The mesh of our finite difference model is aligned with the strike of the fault (see Fig. 2). The vertical boundaries of the model were fixed in the horizontal direction, whereas the lower horizontal boundary was fixed vertically. We imposed a vertical stress on the upper model boundary to simulate the weight of the overburden. Constant pressure boundaries were imposed around the entire model domain. Initial stress conditions were chosen consistent with the regional tectonic setting described for Pohang (Kim et al., 2017; Park et al., 2017, Ge et al., 2019). The initial in-situ stress conditions were assumed to be in a strike-slip tectonic regime, with $\sigma_{Hmax} > \sigma_v > \sigma_{hmin}$ and maximum horizontal stress σ_{Hmax} oriented at an oblique angle (approximately 30°) to the strike of the fault (right-lateral strike slip conditions). Pore pressure gradients were taken hydrostatic. Gradients of the total stresses were 48.3 MPa/km for the maximum horizontal stress, 22.1 MPa/km for the minimum horizontal stress and 26 MPa/km for the vertical stress (Ge et al., 2019).

In our base case scenario, water was injected at the edge of the damage zone at a distance of 50 m from the fault. In reality, injection operations at Pohang have been complex with multiple sequential stimulations on both sides of the fault – whereas the scheme of the final stimulation phase has not been made publicly available. Considering the uncertainties in both the injection patterns and geology and geomechanical parameters of the fractured granites and the fault system itself, we preferred to use a simplified modelling approach, to explore the role of mechanical processes, over a complex model which tries to capture the complete sequence of stimulation. Hence we chose a stimulation scheme in which water was injected at a constant rate of 10 L/s. Duration and total injected volume were approximately similar to the

Table 1
Hydromechanical and geometry properties as input to TOUGHREACT-FLAC3D in the base scenario and sensitivity scenarios for hydromechanical properties of the damage zone.

Base Scenario	E (GPa)	Poisson's ratio (-)	Permeability (m^2)	Biot coefficient (-)	Porosity (-)	Thickness (m)
Fault	33	0.25	2.e-19	0.8	0.001	10
Damage zone	33	0.25	3.e-15	0.8	0.05	50
Matrix	33	0.25	1.e-16	0.8	0.01	–
Sensitivities for hydromechanical properties of damage zone						
Damage zone	Low: 16.5 High: 66					
Damage zone			Low: 1.5e-15 High: 6.0e-15			
Damage zone						Low: 25 High: 100

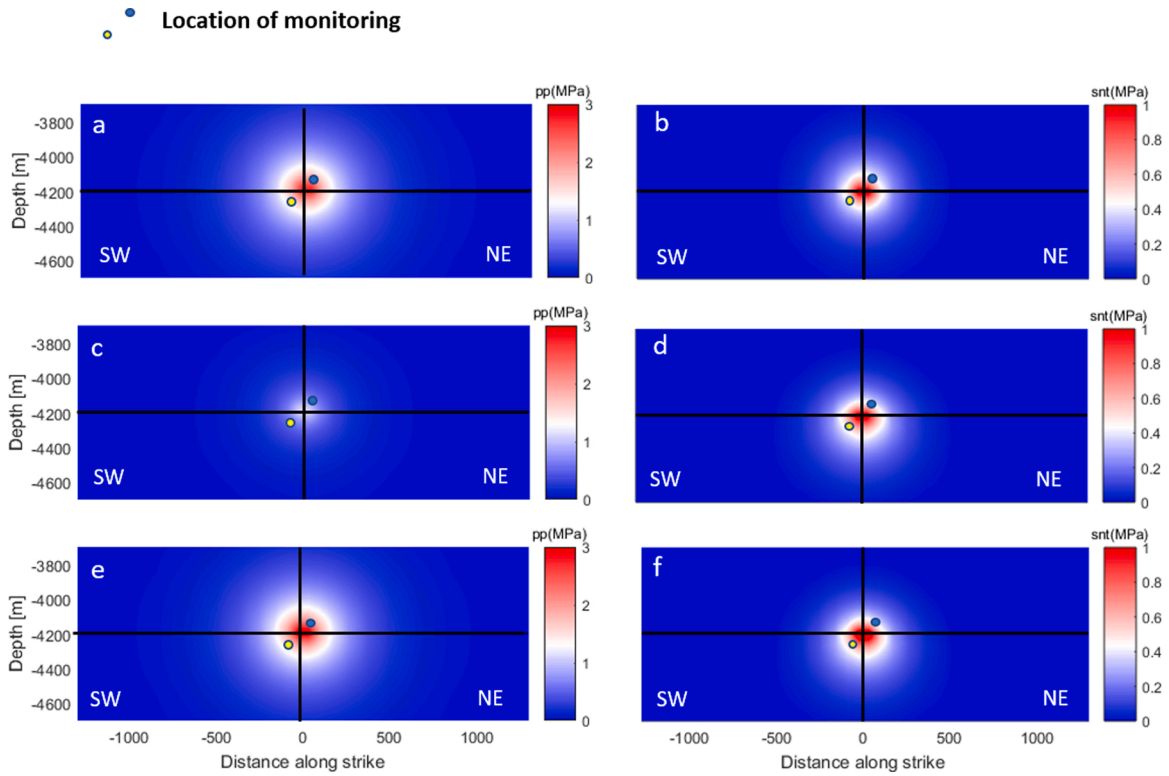

Fig. 3. Changes in pore pressure and total normal stress in the fault, at the end of the injection period: a) pore pressure change for open fault, b) total normal stress change for open fault, c) pore pressure change for sealing fault, d) total normal stress change for sealing fault, e) pore pressure change for partially sealing fault (base scenario) and f) total normal stress change for partially sealing (base scenario). Yellow and blue dot indicate position of monitoring points in Figs. 5 and 6. (For interpretation of the references to colour in this figure legend, the reader is referred to the web version of this article).

duration and total volume injected of a single stimulation phase of well PX-1. We simulated injection of a total volume of 2000 m^3 during a period of just over 55 h, before shut-in of the injection well. The total period modelled was 300 h. This way we capture both the evolution of stresses during injection and after shut-in.

We used the 3D coupled hydro-mechanical model to analyze the impact of fault transmissivity on the (rate of) pore pressure and stress changes on the fault. We chose a base scenario of a fault with intermediate permeability (partially sealing fault). Permeabilities of fault core, damage zone and matrix rocks were based on values given in Ge et al., 2019. As two end members for the permeability of the fault core, a low-permeability fault (sealing fault) and a high-permeability fault (open fault) were modelled. In addition, we analyzed the sensitivity of the fault pore pressure and stress changes to variations in hydromechanical and geometrical properties of the damage zone. The input hydromechanical and geometrical model properties of fault, damage zone and matrix for the base and sensitivity scenarios are summarized in Table 1. In all cases, fault, damage zone and rock matrix had uniform permeability, porosity and elastic properties. We modelled the rocks as a single porous medium, without fractures.

We monitored the spatial and temporal evolution of pore pressures and stresses on the fault resulting from our model calculations. Coulomb stress changes ($\Delta\tau_{cs}$) can be derived from changes in pore pressures and normal and shear stresses on the fault plane. They result from an increase in pore pressures, due to diffusion of pressures into the fault (here referred to as the 'direct pore pressure effect') and/or from poroelastic stress changes, caused by the deformation of the rocks. In terms of total stress, shear stress and pressure, we can write Coulomb stress changes as:

$$\Delta\tau_{cs} = (\Delta\tau_s - \mu\Delta\sigma_n + \mu\Delta P) \quad (1)$$

Where $\Delta\tau_s$ denotes the change in shear stress, $\Delta\sigma_n$ the change in total normal stress on the fault, μ is fault friction coefficient and ΔP is the pore pressure change in the fault. Positive Coulomb stress changes indicate a destabilizing stress path on the fault; negative Coulomb stress changes indicate stabilization. The first two components on the right-hand side in Eq. (1) denote the contribution of poroelastic stress changes on the fault; the last component $\mu\Delta P$ gives the contribution of the 'direct pore pressure effect'.

From the evolution of Coulomb stress changes over time we obtained Coulomb stressing rates, which we then used to derive relative seismicity rates, based on the theory of rate-and-state seismicity by Dieterich (1994):

$$\frac{dR}{dt} = \frac{R}{t_a(t)}\left(\frac{\dot{\tau}_{cs}}{\dot{\tau}_0} - R\right) \quad (2)$$

where the Coulomb stress rate is defined as:

$$\dot{\tau}_{cs} = \dot{\tau} - [\mu(t) - \gamma]\dot{\sigma}_n' \quad (3)$$

with $\dot{\tau}$ is the shear stress rate, $\dot{\sigma}_n'$ is the effective normal stress rate, $\mu(t)$ is the coefficient of fault friction, in which (t) denotes that this coefficient depends on the temporal evolution of shear stress over normal stress, and γ is a constitutive parameter (zero in this study). R is the relative seismicity rate, i.e. the seismicity rate divided by background seismicity rate, $\dot{\tau}_0$ is the tectonic stressing rate, and t_a(t) is a characteristic time decay which corresponds to the time scale of decay of the aftershock rate following a main shock back to the background rate. $t_a(t)$ depends on background stressing rate, fault parameter A (which quantifies the direct effect of rate and state friction behavior of the fault) and the temporal evolution of normal effective stress σ_n' :

$$t_a = A\frac{\sigma_n'}{\dot{\tau}_0} \quad (4)$$

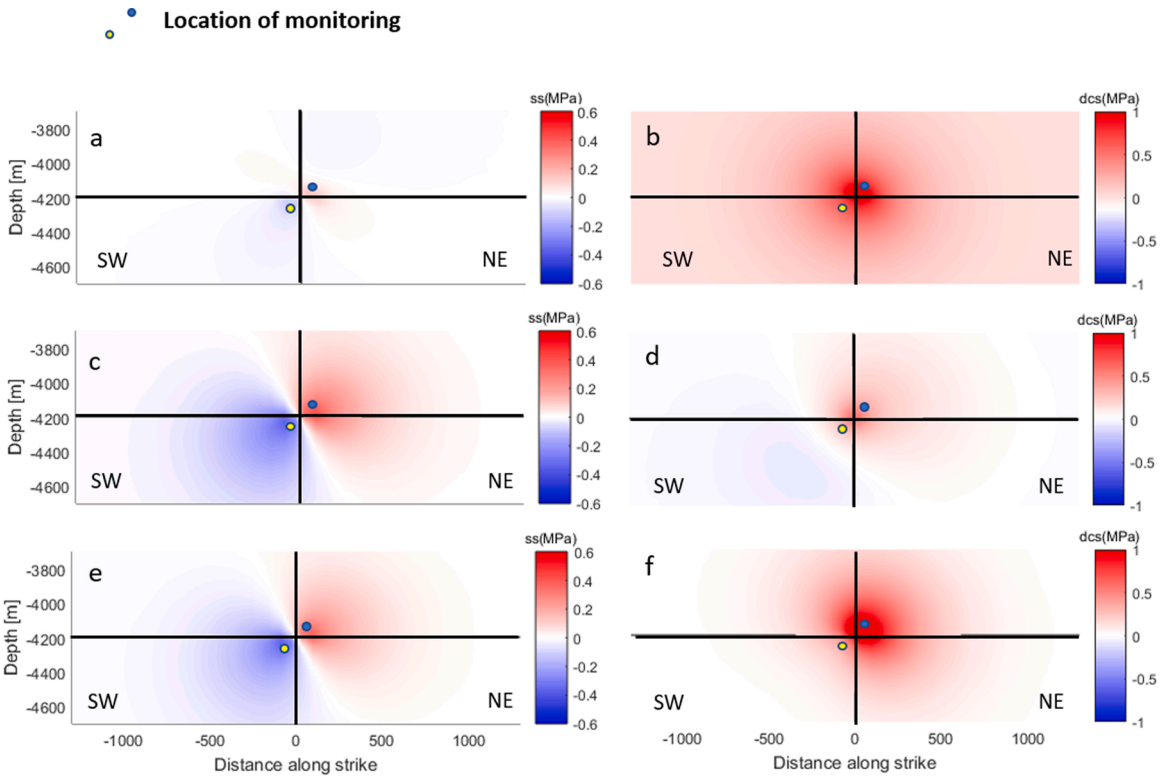

Fig. 4. Changes in shear stress and Coulomb stress at the fault, at the end of the injection period: a) shear stress change for open fault, b) Coulomb stress change for open fault, c) shear stress change for sealing fault, d) Coulomb stress change for sealing fault, e) shear stress change for partially sealing fault (base scenario) and f) Coulomb stress change for partially sealing (base scenario). Yellow and blue dot indicate position of monitoring points in Figs. 5 and 6. (For interpretation of the references to colour in this figure legend, the reader is referred to the web version of this article).

We assumed $A = 0.001$ (Marone, 1998), and $\dot{\tau}_0 = 0.001$ MPa/yr (that is appropriate for a stress drop of 1 MPa every 1000 years). As pointed out by Heimisson and Segall (2018), spatio-temporal changes in $\dot{\sigma_n}$ need to be honored when the magnitude of these changes is relatively high compared to the initial value. Even while in our case the changes in $\dot{\sigma_n}$ are much smaller (~1 MPa) than the pre-injection initial value (~80 MPa), we decided to follow the approach of Rubin and Ampuero (2007) and Candela et al. (2019) when solving the ordinary differential equation (Eq. (2)). These changes in $\dot{\sigma_n}$ are honored at three levels:

[1] for the $\dot{\sigma_n}$ in the calculation of the Coulomb stressing rate in Eq. (3),

[2] for the $\dot{\sigma_n}$ in the calculation of the coefficient of friction in Eq. (3) as defined as $\tau/\dot{\sigma_n}$,

[3] for the $\dot{\sigma_n}$ in the calculation of t_a in Eq. (4).

4. Modelling results

Based on Eq. (1), we can unravel the effect of direct pressure changes and poroelasticity on Coulomb fault stressing. Figs. 3 and 4 show the spatial distribution of pore pressure changes in the fault as well as the associated total normal stress, shear stress and Coulomb stress change for the open (Sc1), sealing (Sc2) and partially sealing fault (base scenario), at the end of the 55 h injection period. At the end of injection, pressures in the partially sealing fault core are slightly higher than in the open fault, since the fault acts as a baffle for flow and increases the pressures in the hanging wall block. Pore pressure changes in the sealing fault core are significantly smaller, as the rate of pressure diffusion into the low-permeability fault core is much slower. We point out that we evaluated the pore pressures within the fault core because we assumed that slip localizes in the fault core. For slip localization at the interface between fault core and damage zone, pressures should be evaluated in the damage zone. In that case the amount of pressure increase for the sealing fault would have been higher, i.e. of the same order of magnitude as for the partially sealing fault. We will come back to the effect of the choice of slip localization at the end of this section and in the discussion.

Total normal stress changes, caused by the volumetric expansion of the rocks are similar for the three scenarios. Changes in shear stresses in the open fault are much smaller than for the faults with lower transmissivity. This can be explained by the fact that for the open fault, pore pressure changes occur in both the foot- and hanging wall block, and cause rock volumes on both sides of the fault to expand. This results in only small differential movements along the fault and therefore in relatively small changes in shear stress. For the sealing fault and to a lesser extent also for the partially sealing fault, poroelastic volumetric expansion of the rocks occurs predominantly in the hanging wall block of the fault. This causes additional shear stresses on the fault; more for the sealing fault than for the partially sealing fault. On the upper segment of the fault above and to the NE of the injection well, induced shear stresses are added to the shear stresses already present from the tectonic loading. The increments in induced shear stresses on the lower and SW fault segment however counteract the in-situ tectonic shear stresses.

Changes in total normal stress, shear stress and pore pressure add up to the Coulomb stress changes (Fig. 4). Coulomb stress changes are largest for the partially sealing fault, even while we observe less destabilization in the lower SW fault segment. Fig. 4d reveals a significant area of stabilization at the lower SW fault segment in case of the sealing fault. Coulomb stress changes in that case are smaller due to the smaller contribution of the pore pressures to fault stressing. No stabilization is observed for the open fault, where the contribution of pore pressures is dominant. Again, here we emphasize that we assume slip localization in the fault core. For slip localization at the interface between the fault core and damage zone, pore pressure changes would also dominate Coulomb

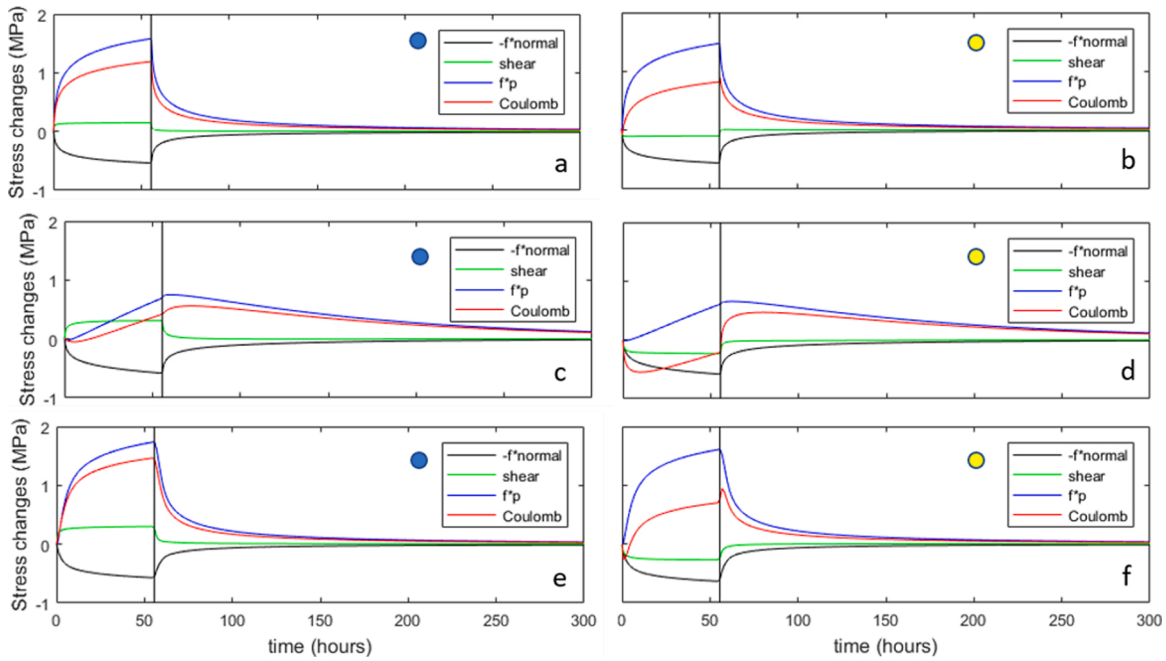

Fig. 5. Contribution of changes in pore pressure, total normal stress and shear stress to Coulomb stress change for a) open fault, upper NE fault segment, b) open fault, lower SW fault segment c) sealing fault, upper NE fault segment, d) sealing fault, lower SW fault segment, e) partially sealing fault (base scenario), lower SW fault segment and f) partially sealing (base scenario) fault, lower SW fault segment. Blue and yellow dots indicate monitoring locations, see also Figs. 3 and 4. Vertical black line represents shut-in time. (For interpretation of the references to colour in this figure legend, the reader is referred to the web version of this article).

stress changes for the sealing fault.

Fig. 5 a–f shows the contribution of individual components to the Coulomb stress changes in time. We plotted the temporal evolution at two locations: 1) in the NE fault segment above the injection level (left) and 2) in the SW fault segment below the depth of injection (right). Again, Fig. 5a and b reveal that direct pore pressure effects dominate the response of the open fault (Sc1), although the evolution of shear stress locally tempers the Coulomb stress increase in the SW fault segment. Both locations reveal an increase of Coulomb stress up to the moment the well is shut-in. At shut-in, a small and narrow peak in Coulomb stresses is observed at location 2, due to a rapid decline of poroelastic normal stress, simultaneous increase of shear stress and a delayed response of the pressures in the fault. Almost immediately after shut-in the Coulomb stress rapidly declines, resulting in a stabilization of the open fault at both locations.

For the sealing fault (Sc2), the pore pressures rise only gradually after the onset of injection. Coulomb stress changes at location 1 are positive at the end of injection, but much smaller than in case of the open fault. At location 2, the combination of low diffusion rate into the fault core, rapid increase of clamping normal stress, and shear stress change which counteracts the tectonic shear stress results in a local stabilization during injection. Coulomb stresses after shut-in at location 2 are again dominated by a slow decline of pore pressures, and a simultaneous, almost immediate release of total normal stresses and associated unclamping of the fault. At the same time, shear stresses rapidly increase after shut-in. This results in a prominent and prolonged increase of Coulomb stresses after shut-in (Fig. 5d).

For the partially sealing fault (base case) the temporal development of pressure and poroelastic stress changes during injection resembles the trend of the open fault. As the fault forms a baffle for flow, pressure build-up in the hanging wall block of the fault at the end of injection is larger than in case of the open fault. Even though diffusion into the fault core is slower, pressures in the fault at the end of injection are slightly higher than for the open fault. We observe a peak in Coulomb stresses

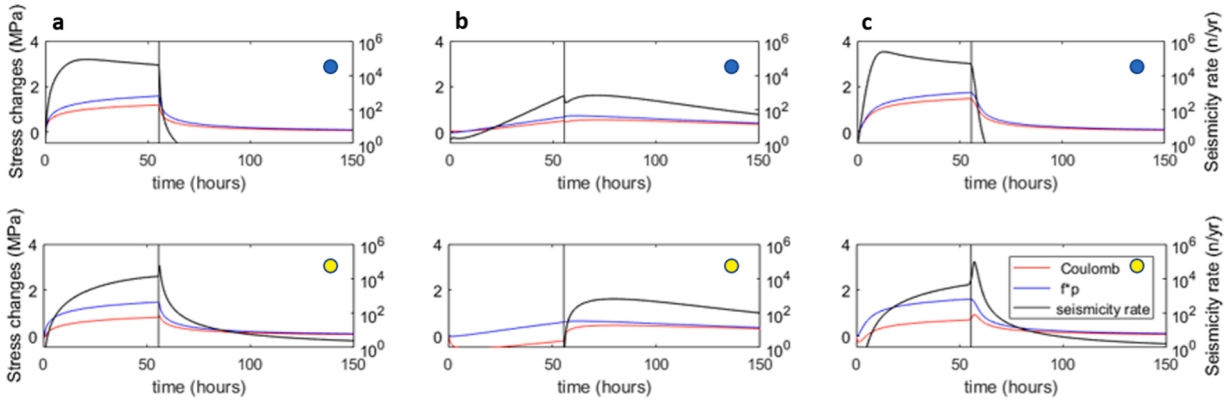

Fig. 6. Slip localization within the fault core: Pore pressure change, Coulomb stress change and relative seismicity rate versus time, for a) open fault, b) sealing fault and c) partially sealing fault (base scenario). Values are plotted for the fault locations in the NE (blue dot) and SW (yellow dot), for location see Figs. 3 and 4. Black vertical line indicates the timing of shut-in. (For interpretation of the references to colour in this figure legend, the reader is referred to the web version of this article).

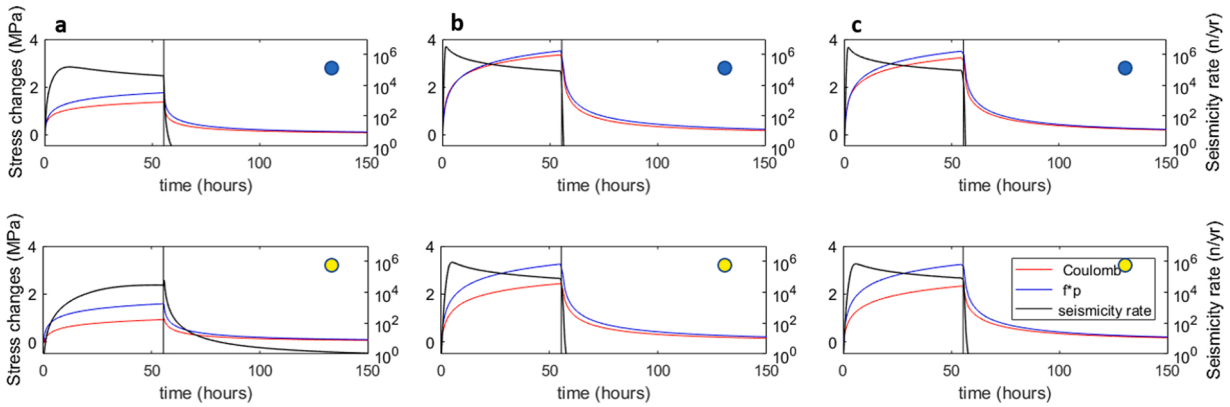

Fig. 7. Slip localization at the interface between the damage zone in the hanging wall block and the fault core: Pore pressure change, Coulomb stress changes and relative seismicity rates versus time, for a) open fault, b) sealing fault and c) partially sealing fault (base scenario). Values are plotted for the fault locations in the NE (blue dot) and SW (yellow dot), for location see Figs. 3 and 4. Black vertical line indicates the timing of shut-in. (For interpretation of the references to colour in this figure legend, the reader is referred to the web version of this article).

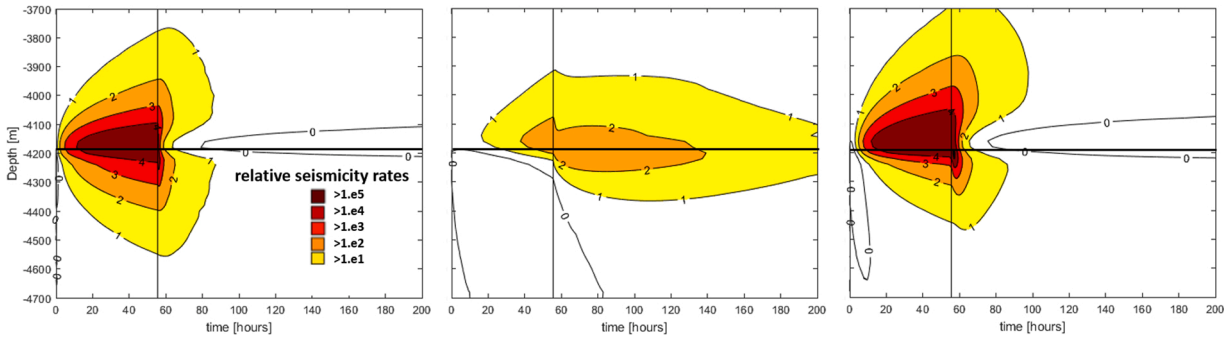

Fig. 8. Relative seismicity rate versus time for 3 scenarios of fault permeability. Seismicity rates on a line along the dip of the fault, intersecting the fault location with maximum seismicity rates, a) open fault (Sc1), b) sealing fault (Sc2), c) partially sealing fault (basecase).

just after shut-in of the injection well, resulting from a relatively slow decline of pore pressures, and a sudden release of poroelastic stresses. Again, we observe the additional contribution of shear stresses to loading after shut-in at fault location 2, as poroelastic shear stresses during injection were stabilizing the fault (Fig. 5f).

From the evolution of Coulomb stress changes we derived Coulomb stressing rates and associated seismicity rates. In Fig. 6 the total Coulomb stress changes and seismicity rates are picked for the same locations as before. In Fig. 8 we plot the temporal evolution of seismicity rates along a line closest to the injection point, and oriented downdip along the fault plane. We find a distinct spatio-temporal evolution of seismicity for the three cases, dependent on fault transmissivity.

For the open fault (Figs. 6a and 8 a), the seismicity rate peaks within the first few hours after injection starts, being dominated by the rapid diffusion of pore pressures into the fault core. Increased seismicity rates occur in both the upper and lower segment of the open fault, and seismicity spreads along the fault plane with ongoing pore pressure diffusion. Shut-in of the injection well results in an aseismic zone in the near-well area of the open fault, which extends further outwards in time.

In case of the sealing fault (Figs. 6b and 8 b), seismicity rates before shut-in evolve slowly and are mainly limited to the upper NE fault segment. After shut-in of the injection well, the lower segment of the sealing fault, which was stabilized due to poroelastic loading during injection, shows an increase of seismicity rates. Compared to the higher permeability fault scenarios, elevated levels of seismicity after shut-in exist for a prolonged period in time.

In case of the partially sealing fault (Figs. 6c and 8 c), the evolution of seismicity mostly resembles the seismic pattern on the open fault. Seismicity is observed soon after the start of injection. During injection elevated seismicity rates mainly occur on the upper NE fault segment. The lower part of the fault is reactivated during the later stages of injection due to ongoing pressure diffusion. The highest event rates occur just after shut-in at the segment of the partially sealing fault below the injection interval.

In all cases, we see a peak in seismicity rate just after shut-in, located at the lower SW fault section. Width and height of the post shut-in peaks increase with decreasing fault transmissivity.

Fig. 7 gives the development of Coulomb stress changes and seismicity rates in time, for a slip surface located at the edge of the fault core at the interface with the damage zone in the hanging wall block of the fault. We assumed that pressure changes in the slip plane are equal to the pressure changes in the damage zone. For the sealing fault and partially sealing fault, this results in a larger influence of pore pressures on fault loading, larger Coulomb stress changes and higher seismicity rates. The temporal evolution of seismicity for the sealing and partially sealing fault structure is quite different from the trends observed in Fig. 6. Unlike the elevated rates that are characteristic for post shut-in seismicity at the slip surface within the fault core, seismicity rates for the low-permeability faults rapidly decline after shut-in. Differences for the open fault are much smaller, since pressure gradients between damage zone and fault core are smaller due to the higher diffusivity of the open fault.

5. Sensitivities for hydromechanical properties of the damage zone

We tested the sensitivity of Coulomb stressing and seismicity rates to the stiffness, permeability and width of the damage zone (see Table 1).

In Appendix A we summarize the results of the sensitivity analysis in terms of contributions of direct pressure and poroelasticity, and related relative seismicity rates. A low transmissivity of the damage zone, defined by either low damage zone permeability or small width, has a large impact on fault Coulomb stressing. Indeed, it magnifies the direct pore pressure and poroelastic loading of the fault. Close to the injection well, steeper gradients and higher pore pressures will build up in damage zones with low permeability and small width than in high-permeability or wide damage zones. These result in a more localized volumetric expansion of the damage zone, and higher shear stresses. Overall, though total normal stresses also increase, the relatively high pore pressures and shear stresses result in higher Coulomb stresses in the fault core for low-permeability or narrow damage zones and a higher associated seismic event rate before shut-in. Changes in damage zone stiffness mainly affect the poroelastic response of the fault, and generally result in relatively small changes in Coulomb stressing rates. A higher stiffness of the damage zone leads to a reduced normal and shear loading of the fault. As both effects counteract, changes in Coulomb stresses are small.

6. Discussion and conclusions

Our hydro-mechanically coupled model of TOUGHREACT and FLAC3D enables the evaluation of the relative contribution of direct pressure and poroelastic effects to fault stressing. Model results indicate that timing, location of seismic events and rates depend on factors like fault transmissivity, position of slip localization, characteristics of the damage zone and the location of injection, either in the hanging wall or footwall block of the fault.

We find that transmissivity of fault and damage zone strongly influences the 3D spatio-temporal pattern of Coulomb stresses and stressing rates, and thereby the spatio-temporal pattern of induced seismicity near the injection well. The presence of a sealing fault structure close to the injection well can increase the relative contribution of poroelasticity to fault loading. The poroelastic response, in combination with a delayed response of pressure diffusion in the low-permeability fault core after shut-in of the injection well, increases the probability of prolonged post shut-in seismicity for the low-permeability fault. Furthermore, a damage zone with low transmissivity promotes high seismicity rates.

In the present model, all rocks have been simulated as homogeneous porous media. Preferential flow through fractures like expected in granodiorites such as encountered in Pohang, has not been simulated. Pore pressure changes in fractured media can lead to the opening or closure of fractures and associated changes in fracture porosity and permeability. Rapid undrained poroelastic loading can also cause fracture deformation, thereby affecting fracture porosity and permeability and inducing additional pore pressure effects (Zbinden et al., 2020). Though effects of fracture deformation and changes in permeability are expected to be most prominent in the near-well area, the effects can alter the contributions of direct pore pressure and poroelastic deformation at the fault. We note that poroelasticity in fractured rocks is non-trivial and requires a large number of generally poorly constrained input parameters. Fracture characteristics and mechanical properties are largely unknown for the Pohang granodiorites, and these effects have currently not been accounted for in our model.

6.1. Implications for Pohang EGS

The model configuration that we used was inspired by the geological and operational setting at the Pohang EGS hydraulic stimulation site. Well test analyses at the Pohang site pointed towards the presence of a low-permeability fault structure in between the two injectors PX-1 and PX-2, in which the injectors occupy two different hydraulic regimes. Ge et al. (2019) and Bethmann et al. (2019) reported a clear distinction between the seismic clouds induced by the stimulations in PX-1 and the ones induced by the stimulations in PX-2 (see Fig. 1). They also reported similarities between the waveforms of the foreshocks of the main M 5.5 event, and the events of the PX-2 seismic cloud. No such similarities were found for seismic events in the PX-1 cloud. Based on these observations, and corroborated by hydraulic modeling, Ge et al. (2019) concluded that the reactivation of the fault and main seismic event had been triggered by pressure diffusion related to the PX-2 stimulations. Modelling results in Chang et al. (2020) on the other hand suggest that the cumulative and combined effect of poroelasticity and pore pressure diffusion from multiple stages of injection in both wells PX-1 and PX-2 had caused seismic events of magnitudes $M_w > 3$ at the Pohang EGS site.

Figs. 6 and 7 revealed that direct pore pressure effects are dominant when slip localizes at the interface between core and damage zone, whereas the relative importance of poroelastic effects increases for slip localization in the fault core. For slip along the edge of the fault core, the seismicity rate peaks at an early stage of injection and it is higher than in case of slip localization within the fault core. The choice of the slip location thus has a large effect on the relative contribution of pore pressure diffusion and poroelastic deformation to fault loading. We note that the process of slip localization in faults under ambient pressure changes is still poorly understood and different perspectives for the choice of slip localization have been described in literature. Jha and Juanes (2014) advocate to evaluate the fault stability, using the maximum pore pressure encountered at the fault section. This implies that the slip surface should be able to switch sides, when maximum pore pressure switches from one side of the fault core to the other. Zbinden et al. (2020) assume slip to localize at the interface between fault core and damage zone, and evaluate pore pressures in the damage zone at the side of the fault closest to the injection well. Our models indicate that elevated stressing and seismicity rates are not necessarily limited to the edge of the fault zone.

The seismic response to stimulation activities in well PX-2, as described by Ge et al. (2019) and Bethmann et al. (2019), points towards a localization of slip near the footwall block, with direct pressure effects being the main loading mechanism for the PX-2 stimulation. If indeed slip largely localized at the side of the footwall block, we consider the model based on slip localization in the fault core (at the side of the footwall block) as more representative for the PX-1 stimulation, since PX-1 is located in the hanging wall block. The latter shows that timing, location and rates of seismicity related to PX-1 stimulation depend on the interaction between pressure diffusion and poroelastic deformation. Poroelastic stresses during the PX-1 stimulation tend to stabilize part of the lower SW fault section, whereas a low-permeability fault core promotes elevated levels of seismicity rates for a prolonged period after shut-in.

Our conceptual model of a low-transmissivity fault close to an injector shows that the interplay between pressure diffusion and poroelasticity can result in a different spatial and temporal pattern for the PX-1 and PX-2 seismic clouds - specifically during the injection activities and immediately after shut-in, when the poroelastic effects are most significant. Differences between the seismic response of the fault caused by the PX-1 and PX-2 stimulations on either side of the fault are amplified by the presence of the low-permeability fault structure. It was shown that fault segments, which respond in an aseismic manner during injection, may destabilize after shut-in, and thus transfer stresses to other fault segments and/or cause a delayed response in seismicity. Overall our modelling results demonstrate that the quantitative understanding of the stress and seismicity response upon injection operations such as in Pohang EGS requires the incorporation of poroelastic effects.

Author statement

Hereby we certify that all authors have seen and approved the final version of the manuscript being submitted. We warrant that the article is the authors' original work, hasn't received prior publication and isn't under consideration for publication elsewhere.

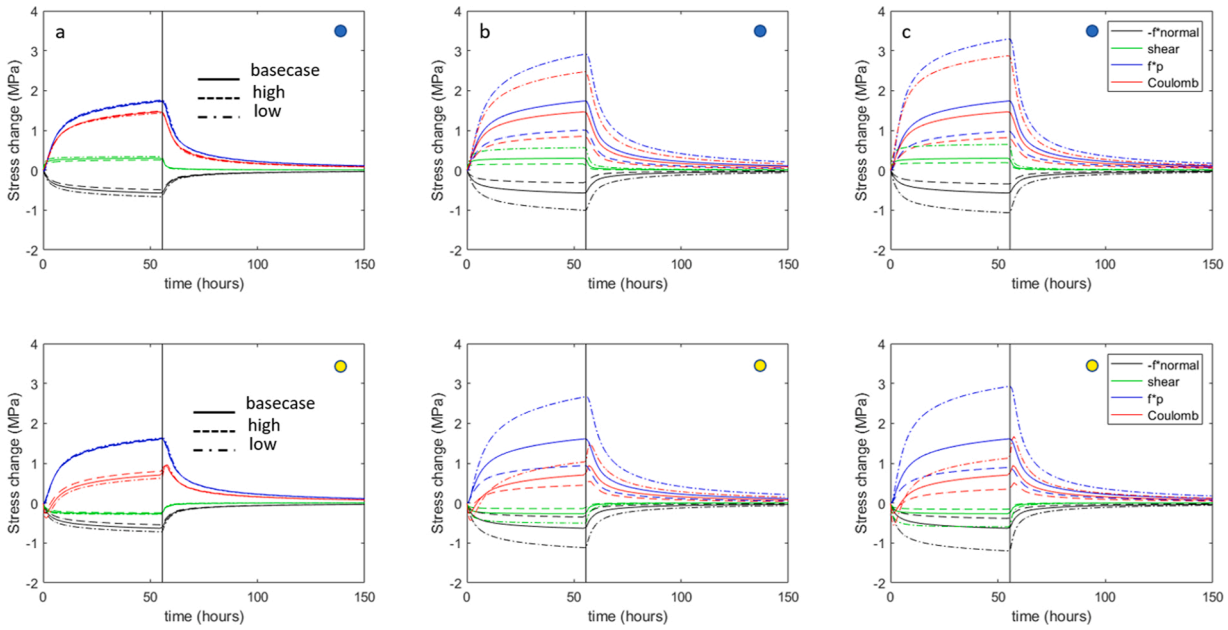

Fig. A1. Results of the sensitivity analysis for parameters of the damage zone, showing pore pressure, normal stress, shear stress and Coulomb stress change for different scenarios. a) stiffness: solid line base case, dot/dash line low stiffness, dashed line high stiffness, b) permeability: solid line base case, dot/dash line low permeability, green line high permeability, c) width of damage zone: solid line base case, dot/dash line small width, dashed line large width. Blue dot indicates monitoring point is located at NE fault segment, yellow dot indicates monitoring point is located at SW fault segment. For location see Figs. 3 and 4. Black vertical line indicates the timing of shut-in.

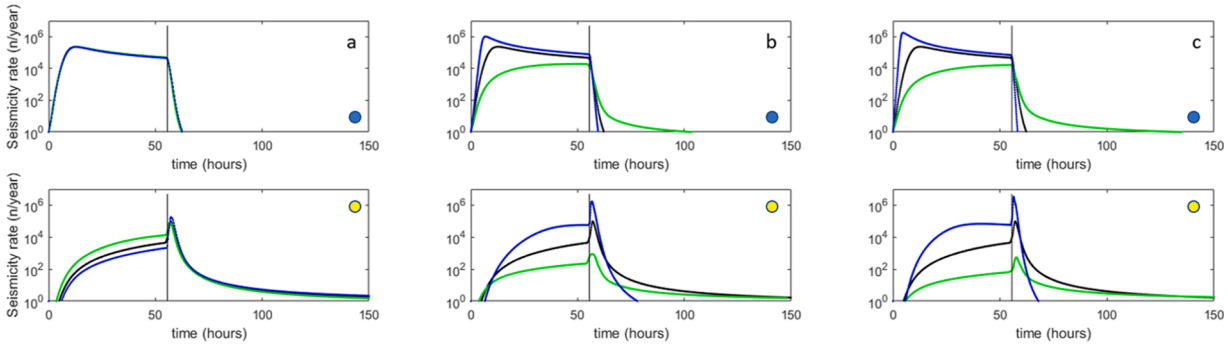

Fig. A2. Results of the sensitivity analysis for parameters of the damage zone, showing relative seismicity rate for different scenarios. a) stiffness: black line base case, blue line low stiffness, green line high stiffness, b) permeability: black line base case, blue line low permeability, green line high permeability, c) width of damage zone: black line base case, blue line small width, green line large width. Blue dot indicates monitoring point is located at NE fault segment, yellow dot indicates monitoring point is located at SW fault segment. For location see Figs. 3 and 4. Black vertical line indicates the timing of shut-in.

Declaration of Competing Interest

The authors declare that they have no known competing financial interests or personal relationships that could have appeared to influence the work reported in this paper.

Acknowledgements

The project leading to part of the results in this article received funding from the European Union's Horizon 2020 research and innovation programme under grant agreement No 691728.

Appendix A. results sensitivity analysis

Figs. A1 and A2.

References

Baisch, S., Weidler, R., Vorös, R., Wyborn, D., De Graaf, L., 2006. Induced Seismicity during the Stimulation of a geothermal HFR Reservoir in the Cooper Basin, Australia. Bull. Seismol. Soc. Am. 96 (6), 2242–2256. https://doi.org/10.1785/0120050255.

Bethmann, F., Ollinger, D., Tormann, T., 2019. Seismicity Analysis With Spatial or Temporal Relation to the Deep Geothermal Project in Pohang During 2016/2017, DESTRESS Internal Report.

Caine, J.S., Evans, J.P., Forster, C.B., 1996. Fault zone architecture and permeability structure. Geology 24 (11), 1025–1028. https://doi.org/10.1130/0091-7613(1996)024<1025:FZAAPS>2.3.CO;2.

Candela, T., Osinga, S., Ampuero, J.P., Wassing, B., Pluymaekers, M., Fokker, P.A., van Wees, J.-D., de Waal, H.A., Muntendam-Bos, A.G., 2019. Depletion-induced seismicity at the Groningen gas field: coulomb rate-and-state models including differential compaction effect. J. Geophys. Res. 124 (7), 7081–7104. https://doi.org/10.1029/2018JB016670, 2019.

Chang, K.W., Segall, P., 2016. Injection induced seismicity on basement faults including poroelastic stressing. J. Geophys. Res. Solid Earth 121. https://doi.org/10.1002/2015JB012561.

Chang, K.W., Yoon, H., 2018. 3-D modeling of induced seismicity along multiple faults: magnitude, rate and location in a poroelasticity system. J. Geophys. Res. Solid Earth 123.

Chang, K.W., Yoon, H., Kim, Y., et al., 2020. Operational and geological controls of coupled poroelastic stressing and pore-pressure accumulation along faults: Induced earthquakes in Pohang, South Korea. Sci. Rep. 10, 2073. https://doi.org/10.1038/s41598-020-58881-z.

Choi, J.H., Yang, S.J., Han, S.R., Kim, Y.S., 2015. Fault zone evolution during Cenozoic tectonic inversion in SE Korea. J. Asian Earth Sci. 98, 167–177 doi: 10.10.1016/j.jseaes.2014.11.009.

Dieterich, J., 1994. A constitutive law for rate of earthquake production and its application to earthquake clustering. J. Geophys. Res. 99 (B2), 2601–2618.

Dorbath, L., Cuenot, N., Genter, A., Frogneux, M., 2009. Seismic response of the fractured and faulted granite of Soultz-sous-Forêts (France) to 5 km deep massive water injections. Geophys. J. Int. 177, 653–675, 10.111/j.1365-246X.2009.04030.x.

Ge, S., Giardini, D., Ellsworth, W., Shimamoto, T., Townend, J., 2019. Overseas Research Advisory Committee Report on the Pohang Earthquake.

Grigoli, F., Cesca, S., Rinaldi, A.P., Manconi, A., Lopez-Comino, J.A., Clinton, J.F., Westaway, R., Cauzzi, C., Dahm, T., Wiemer, S., 2018. The November 2017 Mw 5.5 Pohang earthquake: a possible case of induced seismicity in South Korea. Science. https://doi.org/10.1126/science.aat2010.

Heimisson, E.R., Segall, P., 2018. Constitutive law for earthquake production based on rate-and-state friction: Dieterich 1994 revisited. J. Geophys. Res. Solid Earth 123, 4141–4156. https://doi.org/10.1029/2018JB015656.

Hofmann, H., Zimmermann, G., Farkas, M., Huenges, E., Zang, A., Leonhardt, M., Kwiatek, G., Martinez-Garzon, P., Bohnhoff, M., Min, K., Fokker, P., Westaway, R., Bethmann, F., Meier, P., Yoon, K.S., Choi, J.W., Lee, T.L., Kim, K.Y., 2019. First field application of cyclic soft stimulation at the Pohang Enhanced Geothermal System site in Korea. Geophys. J. Int. 217 (May (2)), 926–949. https://doi.org/10.1093/gji/ggz058.

Jha, B., Juanes, R., 2014. Coupled multiphase flow and poromechanics: A computational model of pore pressure effects on fault slip and earthquake triggering. Water Resour. Res. 50 https://doi.org/10.1002/2013WR015175.

Kim, K.H., Ree, J.H., Kim, J.H., Kim, S., Kang, S.Y., Seo, W., 2018. Assessing whether the 2017 Mw 5.4 Pohang earthquake in South Korea was an induced event. et al 2018. Science. https://doi.org/10.1126/science.aat6081.

Marone, C., 1998. Laboratory-derived friction laws and their application to seismic faulting. Ann. Rev. Earth Planet. Sci. 26, 643–696.

Mitchell, T.M., Faulkner, D.R., 2009. The nature and origin of off-fault damage surrounding strike-slip fault zones with a wide range of displacements: a field study from the Atacama fault system, northern Chile. J. Struct. Geol. 31, 802–816.

Rubin, A.M., Ampuero, J.P., 2007. Aftershock asymmetry on a bimaterial interface. J. Geophys. Res. 112, BO5307. https://doi.org/10.1029/2006JB004337.

Segall, P., Lu, S., 2015. Injection-induced seismicity: Poroelastic and earthquake nucleation effects. J. Geophys. Res. Solid Earth 120, 5082–5103.

Taron, J., Elsworth, D., 2010. Coupled mechanical and chemical processes in engineered geothermal reservoirs with dynamic permeability. Int. J. Rock Mech. Min. Sci. 47, 1339–1348.

Zbinden, et al., 2020. Hydromechanical modeling of fault reactivation in the St. Gallen Deep Geothermal Project (Switzerland): poroelasticity or hydraulic connection? Geophys. Res. Lett. 47 https://doi.org/10.1029/2019GL085201 e2019GL085201.